

# Compensation of RF Field and Receiver Coil Induced Inhomogeneity Effects in Abdominal MR Images by A Priori Knowledge on the Human Adipose Tissue Distribution

Christian Würslin, Dipl-Ing,<sup>1,2\*</sup> Fabian Springer, MD,<sup>1</sup> Bin Yang, PhD,<sup>2</sup> and Fritz Schick, MD, PhD<sup>1</sup>

**Purpose:** To reliably compensate bias field effects in abdominal areas to accurately quantify visceral adipose tissue using standard T1-weighted sequences on MR scanners with up to 3 Tesla (T) field strength.

**Materials and Methods:** Compensation is achieved in two steps: The bias field is first estimated by picking and fitting sampling points from the subcutaneous adipose tissue, using active contours and a thin plate fitting spline. Then, additional sampling points from visceral adipose tissue compartments are detected by thresholding and the bias field estimation is refined. It was compared with an established method using a simulated abdominal image and real 3T data.

**Results:** At low bias field amplitudes (40–50%), the simulation study showed a good reduction of the mean coefficients of variance (CV) for both approaches (>80%). At higher amplitudes, the CV reduction was significantly higher for our approach (83.6%), compared with LEMS (54.3%). In the real data study, our approach showed reliable reduction of the inhomogeneities, while the LEMS algorithm sometimes even amplified the inhomogeneities.

**Conclusion:** The proposed method enables accurate and reliable segmentation of abdominal adipose tissue using simple thresholding techniques, even in severely corrupted images slices, obtained when using high field strengths and/or phased-array coils.

**Key Words:** bias field; intensity correction; visceral adipose tissue; abdomen

**J. Magn. Reson. Imaging 2011;000:000–000.**

© 2011 Wiley-Liss, Inc.

AS THE WORLD-WIDE occurrence of overweight and metabolic diseases as type 2 diabetes is rising (1,2), programs for measuring body distribution of fatty tissue to assess individual risk factors or to monitor effects of lifestyle interventions become more and more popular. To be able to classify the degree of obesity and to verify intervention response, relatively simple anthropometric measures such as body mass index (BMI) or the waist-to-hip ratio have been used frequently (3). However, these methods can not accurately quantify the body composition, e.g., the amount of adipose tissue (AT) compared with the amount of lean tissue (LT). To achieve a further refinement of the estimated body composition, straight-forward methods such as electrical impedance or underwater weighting analysis can be used, allowing to quantify the relative amount of AT quite accurately (4). However, studies show that different AT compartments have very different impact on metabolism (5,6). Visceral AT (VAT) seems to have great impact, showing high correlation to manifestation of type II diabetes mellitus, metabolic syndrome and the risk of heart failure (7–9). Thus, many recent articles propose methods for precise quantification of VAT. Computed tomography and magnetic resonance imaging (MRI) are used for this purpose and their validity has been shown (10,11) but due to its avoidance of ionizing radiation, MRI is the only modality, that can be used for screening and intervention monitoring purposes in a safe way.

In this context, several MR sequences have been proposed to achieve precise quantification of fatty tissue from MRI. Image acquisition is usually accomplished by 2D T1-weighted spin echo (SE) techniques in transverse plane (12–14), because susceptibility induced signal voids are compensated by spin-echo signal refocusing. Some recent studies also propose image acquisition using gradient echo (GE) sequences, yielding higher signal-to-noise ratio (SNR) in the same acquisition time (15,16), and Dixon based fat-water separation techniques (17,18). However, the use of GE sequences might result in locally reduced signal

<sup>1</sup>Section on Experimental Radiology, Department of Diagnostic and Interventional Radiology, University of Tübingen, Tübingen, Germany.

<sup>2</sup>Chair of System Theory and Signal Processing, University of Stuttgart, Stuttgart, Germany.

Contract grant sponsor: *fortüne*; Contract grant number: 1838-0-0 (Juniorvertrag).

\*Address reprint requests to: C.W., Section on Experimental Radiology, Department of Diagnostic and Interventional Radiology, Hoppe-Seyler-Str. 3, 72076 Tübingen, Germany.  
E-mail: christian.wuerslin@med.uni-tuebingen.de

Received December 7, 2010; Accepted May 23, 2011.

DOI 10.1002/jmri.22682

View this article online at [wileyonlinelibrary.com](http://wileyonlinelibrary.com).

intensity or even signal voids especially in regions close to air containing cavities or in areas with trabecular bone. Dixon techniques for separation of fat and water signal contributions are not available on all scanners, because suitable recording of several images and appropriate postprocessing is not available on many sites. Furthermore, SNR per measuring time is relatively low for Dixon or modern IDEAL sequences.

To identify and quantify different AT compartments, the images have to be postprocessed. In early approaches, this quantification was done manually using threshold values to separate AT from LT and drawing a contour to separate VAT from the remaining AT compartments (12,19). The high amount of user interaction required and the desire to eliminate inter-user variations in the quantification process lead to the development of (semi-) automated quantification procedures. First, the task of separating AT from LT and background (BG) has been implemented to be performed automatically either by clustering algorithms (e.g., fuzzy-c-means [FCM]) (20), histogram analysis (15,21), Gaussian mixture modeling (22) or combinations of these methods (14). More recently, the task of separating subcutaneous AT (SAT) from VAT compartments has also been automated in several approaches using either morphological operations (21) or active contour algorithms (14,20,23).

All these quantification procedures have in common that they rely on a high contrast between AT and LT to accurately categorize each pixel into one of the two tissue classes. This holds true whether the threshold is chosen manually or found in an iterative way by a pattern recognition algorithm. Relatively constant signal yield in the entire volume of interest can be gained by MRI, if first, all relevant parts of the body can be excited by a homogeneous transmitter field  $B_1$ , and second, the receiver coil characteristics is homogeneous for the recorded volume. The latter condition is given for a large single volume coil which cannot provide high sensitivity at the same time. Spatial signal intensity of one distinct type of tissue becomes much more inhomogeneous in abdominal images, if signals are acquired on an MR unit operating at higher field strengths ( $B_0 = 3.0\text{T}$  and more). Additionally, array receiver coil systems with clearly improved sensitivity compared with single volume coils show pronounced inhomogeneities in their spatial sensitivity characteristics dependent on the geometrical arrangement applied for each individual examination.

Thus, in many cases intensity inhomogeneities (IIHs) in the images are strong enough to cause a significant overlap of different tissue classes in terms of brightness. This makes it impossible to correctly segment them throughout the complete image by applying one single threshold. To compensate for this phenomenon, some methods propose to initially correct the image for the bias field, causing inhomogeneous signal intensities, others propose to modify the clustering algorithm such that the underlying bias field is re-estimated in each clustering iteration (24,25). Most of these image correction schemes have been developed in the context of neuroscience. Using dedicated

volume coils for the head and considering the relatively regular geometry of the head, these images usually suffer from IIHs of up to 40%. The recent tendency to ever higher field strengths, and thus reduced wavelengths, in combination with the desire to image other body parts such as the abdomen and the use of phased-array coils, has led to an increase in IIHs to levels above 80% (26,27). Some approaches are capable to handle even these severe IIHs, however, only in areas of rich high frequency content, such as brain tissue or the neck. In abdominal images, these correction schemes without any prior knowledge are no longer able to correctly and reliably estimate and thus compensate for the bias field, sometimes resulting in even more degraded images. On the other hand, the inclusion of a priori information about the image contents always leads to a limitation of the suggested method to a given application, the benefits, however, are a more robust and accurate estimation.

In this study, we propose a procedure which incorporates a priori-information of the region to be corrected to provide reliable automatic correction of the bias field. The correction procedure is tested regarding improvement of an automatic tissue segmentation procedure; however, it is also useful for processing anatomical abdominal images before visualization on the screen.

## MATERIALS AND METHODS

### *Theoretical Considerations*

The bias field, caused by the superposition of all the degradation effects mentioned above, can be modeled as a smoothly varying, multiplicative field, which degrades an ideal, homogeneous image  $I_R(\vec{x})$  to the measured image

$$I_M(\vec{x}) = I_R(\vec{x}) \cdot B(\vec{x}), \quad [1]$$

where  $B(\vec{x})$  is the bias field and  $\vec{x} = (x, y)^T$  is a coordinate in the 2-dimensional image space. In this, the term “smooth” is an objective measure and, from a system theoretical point of view, describes the maximum spatial frequency occurring in  $B(\vec{x})$ . This parameter is linked closely with the real operating frequency of the MR scanner and its wavelength in water as well as the spatial reception characteristics of the coils being used. Thus, the maximum spatial frequency of the bias field increases when using phased-array surface coils instead of the scanner’s body coil or higher field strengths, where interference phenomena within the body become a matter (28,29). However, even in these cases the maximum frequency should not fall below a spatial wavelength of approximately 8 cm.

Another important parameter to characterize the bias field is its amplitude. It is defined as

$$A = B_{\max} - B_{\min}, \quad [2]$$

where  $B_{\max}$  and  $B_{\min}$  are the maximum and minimum values in  $B(\vec{x})$ , respectively. The value of  $A$  is often expressed as a percentage.

### Correction Scheme

Our approach uses AT areas in transverse abdominal images for bias field estimation. For simplicity, the approach will be denoted by BC-FAT (Bias Correction by Fitting of Adipose Tissue intensity) in the following. The benefits of using the AT compartments for bias field correction are as follows:

First, considering the given application (the segmentation of VAT), AT is likely to have a very high signal (inherent to T1-weighted, T2-weighted, and PD-weighted MRI) and thus a high contrast to surrounding tissues and to noisy background. Second, the high signal intensity of AT results in high SNR in these regions, making noise a negligible factor. Third, the distribution of one specific AT compartment is known a priori: The SAT is surrounding the body right beneath the skin, some other fat tissue compartments with very similar chemical composition are found deeper inside of the abdomen. If an algorithm is able to identify the SAT compartment reliably—an image area consisting of only one, supposedly homogeneous tissue class—the underlying bias field can be estimated directly from the area's intensity.

Therefore, BC-FAT uses active contours (30) as a robust contour tracking mechanism to identify the SAT area and identifies sampling points to estimate a preliminary bias field. In a second step, an image, corrected with this preliminary estimation for the bias field is used to identify VAT compartments deeper inside the abdomen for further refinement of the bias field estimation. The outline of the proposed algorithm is also shown in Figure 1.

#### Preliminary Bias Field Estimation From SAT

The first step is the identification of SAT areas. Because this AT compartment is always found beneath the skin, finding the outer border of the SAT ring is actually the task of identifying the body contour. In a second step, the inner contour of the SAT is detected. These are two tasks that also can be found in some current VAT quantification algorithms, however, only in the context of either quite homogeneous images or after inhomogeneity correction of the image. The expectance of high ITHs in the range of 60–80% create the need for a very reliable contour tracking method, because the magnitude of edges in areas of strong signal attenuation ( $B(\vec{x})$  small) are attenuated as well. Thus, low level image processing procedure such as region growing (stopping at significant image features such as edges) or clustering (requiring homogeneous signal intensity within the same region) are no longer a good choice for the identification of SAT. Active contours, as introduced by Kass et al (30) provide a powerful framework for contour detection and tracking. These contours, that also have been used for the separation of SAT and VAT in some studies mentioned above (14,20,23), are able to lock onto certain image features, e.g., edges. They can be described as a 2D-function  $\vec{v}(s) = (x(s), y(s))^T$ ,  $s = [0 \dots 1]$ , that iteratively adapts to image features as to minimize the objective function

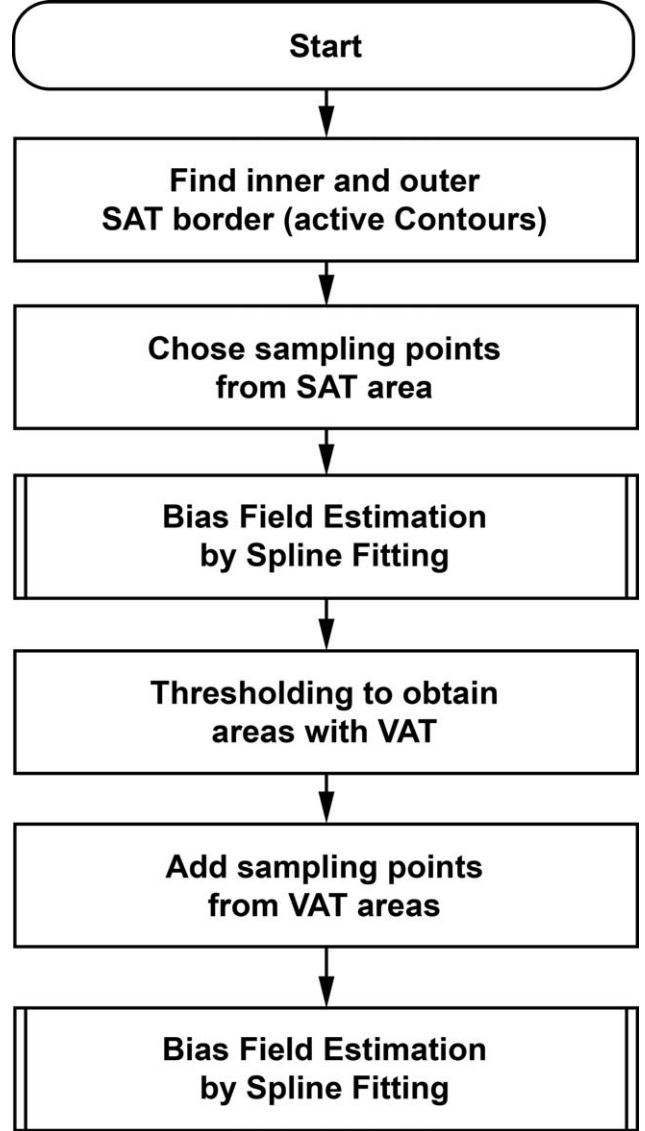


**Figure 1.** Flow diagram of the proposed algorithm.

$$E_{\text{snake}} = \int_0^1 E_{\text{int}}(\vec{v}(s)) + E_{\text{ext}}(\vec{v}(s)) ds, \quad [3]$$

where  $E_{\text{ext}}$  is an external energy which can be derived from an image feature and the internal energy  $E_{\text{int}}$  which provides smoothness constraints to the snakes through weighting parameters  $\alpha$  and  $\beta$  in:

$$E_{\text{int}} = \frac{1}{2} \left( \alpha \left| \frac{d\vec{v}(s)}{ds} \right|^2 + \beta \left| \frac{d^2\vec{v}(s)}{ds^2} \right|^2 \right). \quad [4]$$

Minimization of  $E_{\text{snake}}$  is achieved iteratively by solving equations

$$\begin{aligned} \vec{x}_{t+1} &= (\mathbf{A} + \gamma\mathbf{I})^{-t} (\gamma\vec{x}_t - \vec{f}_x(\vec{x}_t, \vec{y}_t) + \rho\vec{n}_x) \\ \vec{y}_{t+1} &= (\mathbf{A} + \gamma\mathbf{I})^{-t} (\gamma\vec{y}_t - \vec{f}_y(\vec{x}_t, \vec{y}_t) + \rho\vec{n}_y), \end{aligned} \quad [5]$$

Table 1  
Parameters of the Active Contour Algorithm

Step	$\alpha$	$\beta$	$\gamma$	$\rho$	$n_{iter}$	$d_{min}$	$d_{max}$
Body contour detection	0.1	1	5	-0.15	300	3	6
SAT inner border detection	0.1	1	10	-0.15	300	3	6

Where  $\vec{x}$  and  $\vec{y}$  are vectors containing the discretized snake points,  $\mathbf{A}$  is a matrix considering the internal energy and  $\mathbf{I}$  is the identity matrix. Parameter  $\gamma$  is a step size parameter and  $\vec{f}_x$  and  $\vec{f}_y$  reflect the external energy in  $x$ - and  $y$ -direction, respectively. The last term controlled by parameter  $\rho$  is a normal vector, causing the contour to either in- or deflate according to the sign of  $\rho$ .

The main advantage of using these active contours is that the shape of a contour to be found can be restricted, mainly regarding its curvature (parameters  $\alpha$  and  $\beta$ ). This makes the algorithm very robust to noise and incomplete data, e.g., signal voids in certain areas as we would expect them in MR images if corrupted by strong bias fields.

For identification of the body's outer contour, we initialize the contour at the image boundary, far away from the expected target contour. Therefore, the active contour algorithm was used in an extended form, using balloon forces (31), controlled by parameter  $\rho$ . The full list of parameters used in both steps of the SAT detection can be found in Table 1 and an example of the obtained contours can be seen in Figure 2a. The parameters  $\gamma$ ,  $n_{iter}$ ,  $d_{min}$ , and  $d_{max}$  describe step size, number of iterations and minimal and maximal distance between the discrete snake points, respectively. Both steps used the gradient magnitude of the image as external force.

Now, sampling points in the obtained SAT area are chosen to estimate an underlying bias field. The way of choosing these positions can be realized in different ways (e.g., random sampling, sampling on a Cartesian grid, etc.) and is uncritical. The maximum distance between the sampling points, however, has to be limited to not lose any bias field-related information. Considering the Nyquist-Shannon sampling theorem and the assumption, that the minimum spatial wavelength of the bias field will not fall beneath 8 cm, sampling points have to be chosen at least every 4 cm in each direction. In our implementation, we chose the sampling points by transforming the image into polar coordinates, with the body centroid as origin of the coordinate system, and selecting sampling points at 50 equally spaced angles. This leads to a sampling point distance of approximately 18 to 25 mm. At each of these angles, a sampling point was chosen in the middle between the inner and outer SAT border to avoid the consideration of partial volumes. In case, the SAT ring was thick enough, several sampling points were chosen in radial direction with a point-to-point distance of 20 mm (see Fig. 2b).

Having determined this selection of sampling points, a preliminary estimation of the bias field can be done. To get a good estimation within the area enclosed by the SAT (the abdomen), a thin plate smoothing spline is used to fit the bias field

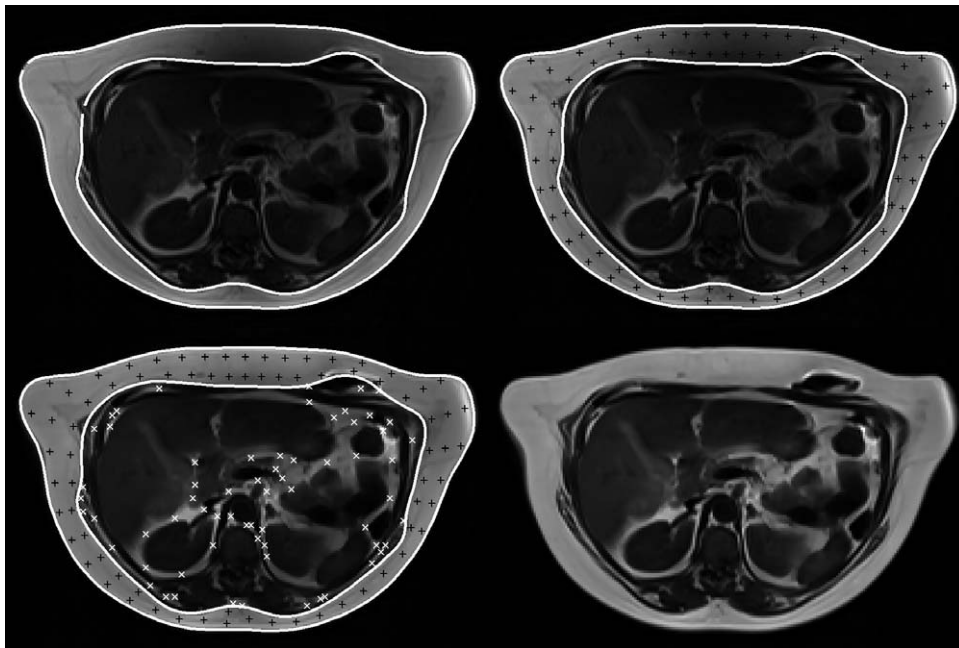


**Figure 2.** Illustration of the algorithm steps: Original image with outer and inner border SAT, detected by active contours (a) choice of sampling points in the SAT (b) image, corrected with the preliminary bias field estimation and choice of sampling points in the VAT (c) corrected image (d).



**Figure 3.** Simulation of the scanner's degradation process: Original simulated abdominal image (a) construction of bias field using a bicubic spline interpolation of knots (dots) with random magnitude (b) application of additive white Gaussian noise (c).

estimation to the sampling points. This spline surface is found by minimizing the cost function

$$J_{\text{Spline}} = p \cdot E(B(\vec{x})) + (1 - p) \cdot R(B(\vec{x})), \quad [6]$$

where  $E(B(\vec{x}))$  is the sum of the squared distance of the spline at the sampling point locations to the value of the sampling points, and  $R(B(\vec{x}))$  is a measure of the spline's roughness. Parameter  $p$  serves as a trade-off parameter between interpolating the sampling points ( $p = 1$ ) and least-squares fitting a plane to the data ( $p = 0$ ). In this application we found  $p = 0.001$  to be a good trade-off for simulated and real bias fields. Other applications (e.g., when using small phased-array coils) will eventually require to alter this value. Using the preliminary bias field, a first corrected image  $I_{\text{pre}}(\vec{x})$  can be calculated according to Eq. [1].

#### Final Bias Field Estimation From All Adipose Tissue Compartments

So far, the estimation of the bias field is only based upon sampling points in the SAT, leaving a large area (inside the ring of SAT), where the bias field is only estimated based on the spline fit. To refine this preliminary bias field, more sampling points in the AT have to be detected at the inner parts of the abdomen and taken into consideration when reestimating the bias field. To find inner AT compartments, the assumption is made, that the image  $I_{\text{pre}}(\vec{x})$  is already compensated for the worst effects of the IIHs and at least parts of the inner AT compartments can be found by simply thresholding  $I_{\text{pre}}(\vec{x})$  at 0.75 times the average intensity of the SAT area. To get a series of sampling points in the newly obtained AT areas, an iterative algorithm is used, which treats all unconnected inner AT regions separately. In each region the pixel with the highest intensity is chosen as a sampling point and the pixel itself and all surrounding pixels in a  $32 \text{ mm} \times 32 \text{ mm}$  area are deleted. This is repeated until the region has vanished.

Having identified sampling points in the SAT and inner AT compartments, (see Fig. 2c), the bias field estimation is refined using the same fitting procedure as described above, except that all sampling points from SAT and inner AT compartments are used (Fig 2d).

#### Validation Process

The algorithm was tested using a simulated abdominal image as well as T1-weighted abdominal SE images of slim and obese volunteers. Its performance was compared with an approach, presented by Salvado et al (27). The simulated abdominal image was used to quantify the algorithm's absolute accuracy by means of pre- and postcorrection in-class coefficient of variance (CV). The CV is defined as the ratio between the standard deviation  $\sigma_X$  and mean value  $\mu_X$  of a random variable  $X$ , i.e.,  $CV = \sigma_X / \mu_X$ . Therefore, it can be used as a measure of the homogeneity of a class, if all pixel intensities of one class are treated as the underlying random variable. The T1-weighted abdominal SE images, acquired with a whole-body 3T scanner containing severe IIHs, served as a benchmark for the algorithm's potential to correct real image data containing a higher count of tissue classes (though many of them underrepresented) and blurry tissue transitions. Furthermore, to make sure that the influence of the imaging modality can be neglected, T1-weighted GE images ( $T_R = 100 \text{ ms}$ ,  $T_E = 2.46 \text{ ms}$ ,  $\alpha = 70^\circ$ , in-plane resolution  $1.7 \text{ mm} \times 1.7 \text{ mm}$ ) were used and the performance of the algorithm was evaluated visually.

#### Simulated Abdominal Image

For the evaluation of the method, a simulated abdominal image was created in close resemblance of a real image scene (Fig. 3a). The image scene was selected because it represents a challenging case, in which the SAT area is not very thick and VAT areas can only be found in the left part of the image. The other side is completely occupied by liver and lung tissue. Thus, BC-FAT is not able to retrieve any bias field information from this area. The underlying anatomical image was acquired on a 3T Magnetom Trio (Siemens Healthcare, Erlangen, Germany) with a Turbo-SE technique. Repetition time was 452 ms and echo time 53 ms, resulting in a T1-weighting, suitable for segmentation of AT. The field of view was  $510 \times 380 \text{ mm}^2$ ; the acquired matrix size was  $256 \times 192$  pixels, resulting in an in-plane resolution of approximately  $2 \times 2 \text{ mm}^2$ . Slice thickness was 10 mm. The image was carefully segmented manually into the five predominant brightness classes BG, muscle, organs, vertebra, and AT and the average

brightness of each region in the real image was assigned to the regions in the image.

The simulated abdominal image could be corrupted by a random bias field and additive white Gaussian noise with arbitrary SNR (expressed as the ratio between the highest image intensity and the standard deviation of the noise). The bias field was constructed by placing knots of a certain distance on a Cartesian grid and assigning random values in the range [0...1] to them (see Fig. 3). In between the knots, the bias field is interpolated using a bicubic spline. Then the bias field was rescaled such that its amplitude inside the tissue area matched the desired bias field amplitude according to equation [2]. To resemble bias fields, observed in abdominal images at 3T, the knots were placed on a 12 cm  $\times$  12 cm grid.

As a measure of the in-class homogeneity, the CV was calculated in each tissue class. Through division by the mean value, the standard deviation values are normalized and allow a comparison between classes with different mean intensities and make the values to be unaffected by scaling. To evaluate the performance of a correction scheme, the CVs before and after correction and the amount of its reduction was calculated in each tissue class. This procedure was repeated 25 times for a given set of parameters (bias field amplitude and SNR) and the average CVs and their average reduction was calculated.

#### *T1-Weighted Abdominal SE Images*

To prove the applicability of the algorithm on real image scenes, 10 abdominal image slices of 10 different normal-weight and obese volunteers (4 female, 6 male, age  $35.1 \pm 5$  y, BMI  $30.4 \pm 4.3$  kg/m<sup>2</sup>) were acquired with the same parameters as the basis for the simulated abdominal image. Especially, images with a high amount of IIHs (as perceived visually) were chosen to challenge the compensation algorithms. To evaluate the algorithm's dependence on the thickness of the SAT area, images with a wide variety of VAT area were used.

In this study, an accuracy analysis using the CVs of different tissue classes is no longer feasible due to the high amount of pixels with partial volumes and the increased number of tissue classes in the image. Therefore, to compare the performance of different correction schemes, the FCM algorithm, which is often used in the context of AT quantification, was used to segment the images into the classes BG, LT and AT after intensity correction. Then, the area of the AT was used as a quality benchmark by comparing it to a gold standard. The gold standard was obtained by a manual bias field correction in each of the 10 images using an in-house developed graphical user interface based on Matlab and subsequent segmentation by FCM. The graphical user interface allows the user to specify a Cartesian grid of knots with arbitrary knot spacing and manually adjust the magnitudes of the knots while interpolating the bias field in between using a bicubic spline. Image intensity could be plotted across arbitrary image lines and columns to have a graphical indicator of the image homogeneity.

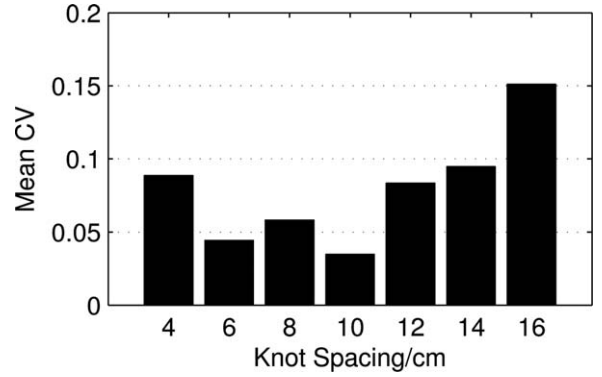


**Figure 4.** The postcorrection mean CVs for different LEMS knot spacing using the simulated abdominal image (bias field amplitude = 50%, SNR = 100).

#### *Comparison Basis: LEMS*

This section will briefly describe the algorithm which was chosen for comparison. The method described as “local entropy minimization with a bicubic spline model” (LEMS) was introduced as a method for the correction of IIHs, mainly induced by phased array coils in the context of characterization of atherosclerosis. However, by adapting knot spacing and iteration count, it is also a good approach for the intensity correction of abdominal cross-sectional images. Like most other image correction schemes, it assumes that the number of tissue classes in an image is finite, thus a homogeneous image should have dedicated peaks in its histogram instead of being flat (uniform distribution). A uniformly distributed (flat) histogram has high entropy, a measure defined as:

$$H = \sum_l \text{PDF}_X(l) \cdot \log(\text{PDF}_X(l)), \quad [7]$$

where PDF is the probability density function (representing the histogram) and  $l$  represents the gray values in an image. A histogram with defined peaks, on the other hand, has low entropy. Therefore, LEMS seeks to minimize the entropy in subareas of the image (locally). The estimation of the underlying bias field is achieved iteratively by changing the bias field estimate at certain points (knots) and interpolating in between, thus incorporating a smoothness constraint. To allow the algorithm to compensate heavy IIHs, we choose the number of possible iterations to 6.

The advantage of the method is certainly its generality, allowing a widespread usage which is already reflected in a variety of publications. The algorithm, however, does not work completely without prior knowledge, but relies strongly on a careful choice of knot spacing. Therefore, in a first step we optimized the algorithm for the given application by evaluating its performance for different knot spacings.

First, this was done for the simulated abdominal image, by sweeping the knot spacing (from 4 cm to 16 cm, 2 cm step size) at fixed bias field amplitude of 50% and SNR of 100 and calculating mean CVs as described above. To see the algorithm's overall

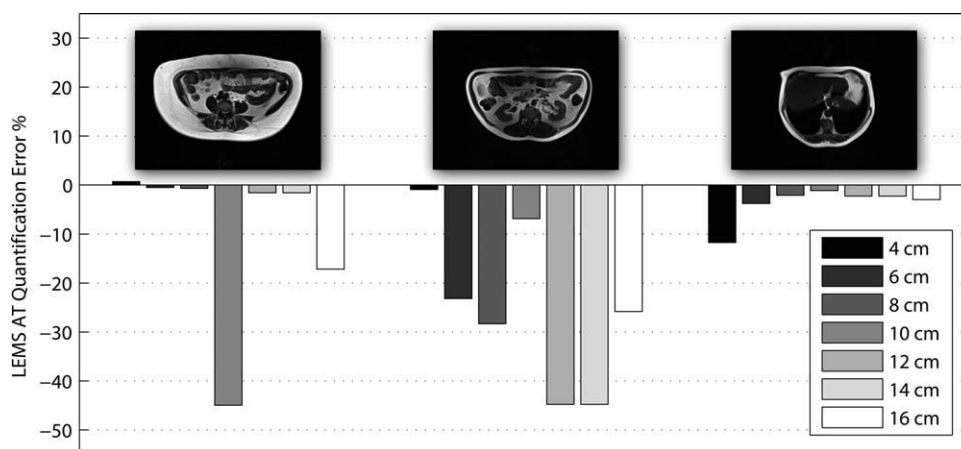


**Figure 5.** The AT quantification error of the LEMS algorithm in three T1-weighted abdominal SE images, depending on knot spacing.

performance at one particular knot spacing, the CVs for the different tissue classes were averaged out in this case and can be seen in Figure 4. It shows a global minimum at knot spacing of 10 cm, which was chosen for the simulated abdominal image study.

To parameterize LEMS for the T1-weighted abdominal SE study, we chose 3 of 10 images (test images 1, 5, and 8) and evaluated the AT quantification error for different knot spacings as described above. The result of this test can be seen in Figure 5. It reveals that the AT quantification error heavily relies on a good choice of the knot spacing. However, the optimal choice may differ heavily even across images, acquired with the same parameters. Furthermore, the relation between knot spacing and quantification error seems to be arbitrary, which is reflected by the large jumps in the graph. Because the overall performance was best for knot spacing of 4 cm, this value was used in the T1-weighted abdominal SE image study.

## RESULTS

### Simulated Abdominal Image Study

The phantom study seeks to evaluate the algorithm's capability of restoring in-class homogeneity depending on initial bias field amplitude and SNR. The first phantom study was done with no noise ( $\text{SNR} = \infty$ ), because the amount of noise clearly biases the CVs. Bias field amplitudes from 40–80% with 10% increments were investigated. For LEMS, a knot spacing of 10 cm was used. Figure 6 shows the CVs of all four tissue classes separately for bias field strength of 60% exemplarily. The bars on the left show the values for the original, uncorrected phantom image, the ones in the middle show the values after LEMS correction and the bars on the right show the values for BC-FAT. It is obvious that both algorithms reduce the CVs of all four tissue classes significantly. For the small vertebra class, the two algorithms are break even, for the three remaining classes, BC-FAT outperforms LEMS. This is most pronounced for the class of AT. The class-dependent differences in the performance of the two algorithms could be observed throughout bias

field amplitudes and SNR levels. So, for lucidity's sake, only the mean CVs across all four tissue classes will be plotted and discussed in the following.

The development of the CVs over the amount of bias field amplitude at infinite SNR can be seen in Figure 7. For each bias field level, the mean CVs for the uncorrected images, the LEMS-corrected images and the images corrected with BC-FAT are shown. At low bias field amplitudes, the difference between LEMS and BC-FAT is not very significant. However, the CVs of the LEMS-corrected images are growing over-proportionally with increasing bias field amplitude, while the CVs of the uncorrected simulated abdominal image (by definition) and of BC-FAT grow nearly linearly with the bias field amplitude. Thus, for strong bias fields, the intensity correction is much more efficient and enables a more accurate AT segmentation using BC-FAT. This tendency can also be seen in the first two rows of Table 2, which show the reduction of the mean CVs by the two approaches as a percentage of the mean CVs in the uncorrected phantom image. These vary significantly for the LEMS

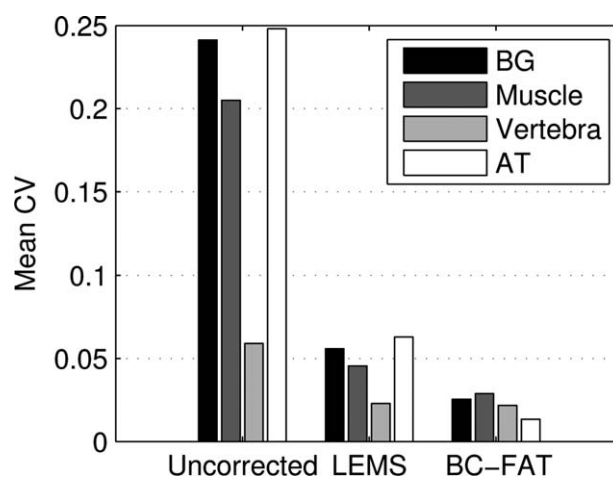


**Figure 6.** Example of a CV plot for all four tissue classes in the simulated abdominal image (bias field amplitude = 60%,  $\text{SNR} = \infty$ ).

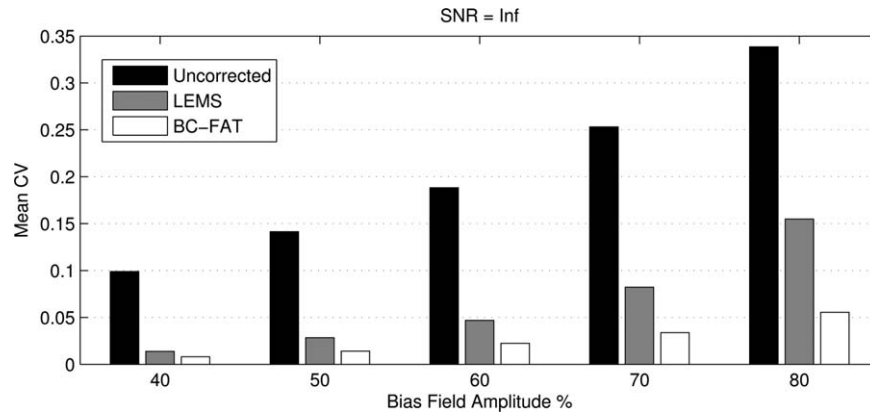


**Figure 7.** Mean CVs in the simulated abdominal image before and after correction depending on the bias field amplitude (SNR =  $\infty$ ).

algorithm (86.2–54.3%) while the values for BC-FAT are less influenced by bias field amplitude and are on a constantly high level (91.9–83.6%).

To investigate the influence of image noise on the intensity correction, we repeated the experiment with SNR values of 100 and 50. The results at SNR value of 100 did not show any significant changes, compared with no noise present (see Table 2). Now, the LEMS algorithm seems to be slightly less influenced by the bias field amplitude than before. Generally, the CV reduction is approximately 10% less than without noise, however, it has to be noticed that the noise by its nature adds a certain “base CV” to all CVs, thus reducing the maximum possible CV reduction.

The mean CVs before and after image correction at a SNR level of 50 are shown in Figure 8. While the two algorithms perform quite similarly to bias field amplitude of up to 60% (certainly also caused by a even higher noise-induced “base CV”), the performance of the LEMS algorithm drastically drops to a value of only 6.3% at an 80% bias field amplitude (compare Table 2).

### T1-Weighted Abdominal SE Image Study

The study with the T1-weighted abdominal SE images examines the AT quantification error in 10 real image slices acquired at 3T, thus corrupted by IiHs. The LEMS knot spacing was set to 4 cm. The AT areas, quantified without bias correction as well as after using manual correction, LEMS and BC-FAT correc-

tion are shown in Table 3 as absolute values. It also lists the absolute deviation from the gold standard and the percentage error. For better visualization, Figure 9 also shows these percentage errors. In the uncorrected images, the AT area is constantly underestimated due to the nature of the bias field. It can be noticed, that in images 4 and 5 the LEMS algorithm even outperforms BC-FAT, however, the error is small in both cases (<4%). On the other hand, in images 8 and 9 it can be observed, that the LEMS algorithm even had a larger error than when quantifying from the uncorrected image, indicating, that the algorithm accidentally merged two different classes. The BC-FAT approach, on the other hand, shows a constant error reduction in all cases. Overall, the mean absolute quantification error was 20.7% when using the uncorrected images for quantification, 4.8% when using the LEMS-corrected images, and 1.3% when using the BC-FAT-corrected images.

To prove the algorithm’s independence of the imaging method, 10 T1-weighted GE images were corrected and the results were checked for failing of the algorithm. All images were corrected in a satisfying way, even though flowing blood had a much brighter intensity than AT in these images, proving the algorithm’s robustness.

## DISCUSSION

With the increasing world-wide prevalence of overweight and obesity, lifestyle intervention and body

Table 2  
Reduction of the CVs by LEMS and BC-FAT

SNR	Algorithm	Bias field amplitude				
		40 %	50 %	60 %	70 %	80 %
$\infty$	LEMS	86.2 %	80.0 %	75.2 %	67.5 %	54.3 %
$\infty$	BC-FAT	91.9 %	90.1 %	88.1 %	86.7 %	83.6 %
100	LEMS	76.1 %	65.6 %	65.2 %	63.1 %	53.4 %
100	BC-FAT	77.4 %	78.8 %	79.1 %	77.8 %	73.6 %
50	LEMS	66.9 %	64.7 %	62.3 %	48.5 %	6.3 %
50	BC-FAT	68.9 %	71.6 %	71.9 %	70.6 %	67.4 %

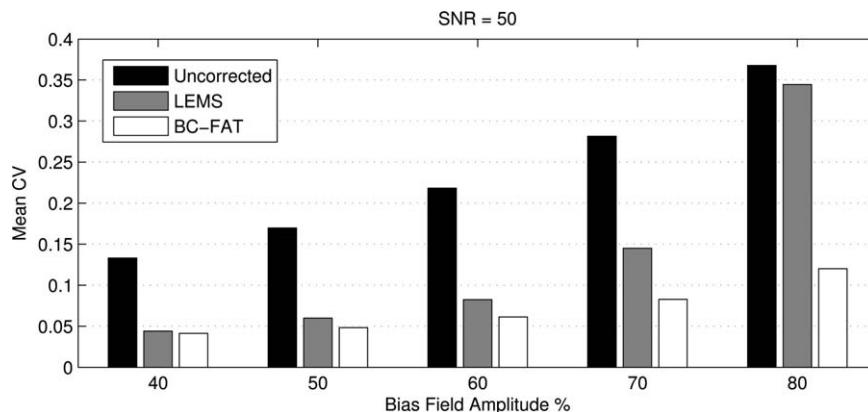


**Figure 8.** Mean CVs in the simulated abdominal image before and after correction depending on the bias field amplitude (SNR = 50).

composition measurement are becoming more and more popular (1,2) and MRI has been used to quantify AT compartments (12,13,17,19,22). To minimize user interaction and cleanse results from inter-observer variations, automatic procedures based on intensity thresholding have been introduced (14–16,21,23). However, MRI intensity variations can corrupt an accurate AT quantification (28,29). In this study, we present an approach for bias field correction in abdominal, non-fat-saturated, transversal image slices. These preconditions clearly limit its application range—the benefits, however, are a much more robust and accurate bias field correction compared with more general approaches, especially when heavily distorted images (acquired at high field and/or with phased-array coils) are subject of correction. This is achieved by considering the anatomy of the imaged body region.

In an simulated abdominal image study, we investigated the performance of the algorithm, compared with an established method from literature. It could be observed, that the inhomogeneity of the AT class (represented by its CV) was corrected most reliably and accurately by BC-FAT (see Fig. 6). An accurate homogenization of the AT class, however, is not a surprise, because interpolating sampling points from

this class is used for bias field estimation. However, the CVs of the three remaining tissue classes in our phantom image were also decreased significantly, even though the absence of AT compartments in the wide parts of the image (e.g., the large area occupied by the liver in the light body half). This shows that the algorithm also achieves good results under challenging conditions, where major parts of the bias field have to be estimated by interpolating remote sampling points.

For our approach, the CV reduction ratio in the simulated abdominal image study with no noise had a constantly high level of more than 80% for bias field amplitudes of up to 80% (see Fig. 7). At SNR of 50, those values were reduced to approximately 70%—here, the CV values, however, were biased by the image noise (see Fig. 8). At low bias field amplitudes of 40%, the difference between BC-FAT and LEMS was only marginal; at 50–60% amplitude, the values differed by approximately 7–13%. At higher bias field amplitudes of over 60%, the differences became very significant (around 20% and higher) and lead to a complete failing of the LEMS algorithm at 80% bias field amplitude and SNR of 50 (note that all these values represent the average of 25 simulation runs for a given set of parameters). However, it has to be

Table 3  
AT Areas in the 10 Test Images Obtained by FCM After Correction

Image	Gold <sup>1</sup>		Uncorrected		LEMS			BC-FAT		
	A [cm <sup>2</sup> ]	A [cm <sup>2</sup> ]	Error [cm <sup>2</sup> ]	Error [%]	A [cm <sup>2</sup> ]	Error [cm <sup>2</sup> ]	Error [%]	A [cm <sup>2</sup> ]	Error [cm <sup>2</sup> ]	Error [%]
1	596.8	497.3	-99.5	-16.7	600.1	3.3	0.6	598.9	2.1	0.4
2	423.5	255.5	-168.0	-39.7	439.2	15.7	3.7	424.0	0.5	0.1
3	406.9	265.4	-141.5	-34.8	385.7	-21.2	-5.2	399.0	-7.9	-1.9
4	561.8	348.5	-213.3	-38.0	579.5	17.7	3.2	580.2	18.4	3.3
5	333.6	250.7	-82.9	-24.9	330.5	-3.1	-0.9	339.8	6.2	1.9
6	158.1	132.5	-25.6	-16.2	150.4	-7.7	-4.9	155.7	-2.4	-1.5
7	189.7	148.0	-41.7	-22.0	187.0	-2.7	-1.4	189.1	-0.6	-0.3
8	246.0	229.7	-16.3	-6.6	219.8	-26.2	-10.7	253.9	7.9	3.2
9	164.9	159.3	-5.6	-3.4	145.5	-19.4	-11.8	165.4	0.5	0.3
10	324.6	309.1	-15.5	-4.8	306.4	-18.2	-5.6	323.8	-0.8	-0.2
Mean				-20.7 ± 13.6			-3.3 ± 5.3			0.5 ± 1.8

<sup>1</sup>Gold-standard obtained by manual correction.

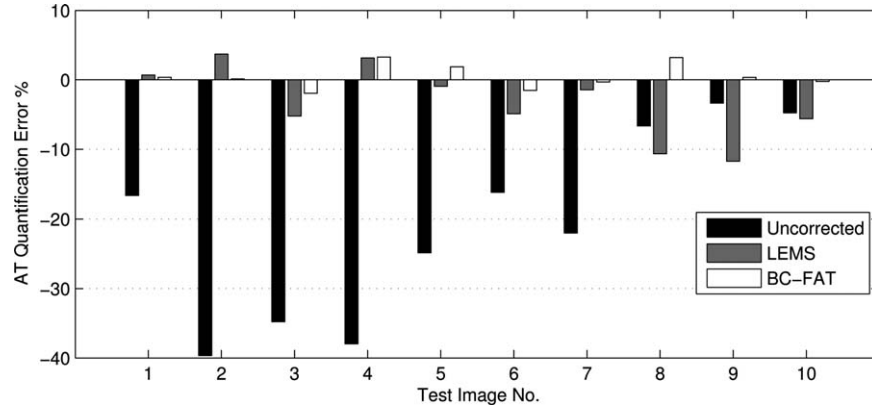


**Figure 9.** Error in the quantification of AT in 10 T1-weighted abdominal SE images compared with the results of manually corrected images slices.

emphasized, that the LEMS represents a very elegant approach for a general problem and is able to reduce moderate bias fields in a much wider application range than our dedicated approach.

In the T1-weighted abdominal SE image study, we evaluated the algorithm's behavior in 10 MR images of slim and obese subjects recorded at 3T using the body coil and compared it with the results of the LEMS algorithm. Images, compensated manually for inhomogeneities served as a gold standard in this study. The mean absolute error of the AT quantification was as low as 1.4% for the BC-FAT approach, compared with 4.8% when using LEMS. While the BC-FAT approach performed quite similar in all images (quantification error below 4% in all 10 image scenes) and was outperformed by LEMS in two images, the LEMS algorithm faced some serious problems in some images (see Fig. 9). In test images 8 to 10, the LEMS result was even worse than compared with AT quantification from the original images. An example of this misleading correction can be seen in Figure 10, where liver tissue is accidentally blended with the noisy lung tissue (test image no. 9). Quantification of AT area in these images was  $147.9 \text{ cm}^2$  in the gold standard,  $143.0 \text{ cm}^2$  in the uncorrected image,  $130.6 \text{ cm}^2$  in the LEMS-corrected image and  $148.4 \text{ cm}^2$  in the BC-FAT-corrected image (the corresponding percentage deviations can be seen in Fig. 9). This behavior can be explained by the strong dependence of the LEMS algorithm on adequate knot spacing. As demonstrated in Figure 5, an optimal choice of this parameter, even for image scenes acquired under the same conditions, was hard to find. This underlines the robustness of the BC-FAT algorithm, which does not rely on such crucial parameters. A qualitative evaluation of the algorithm's performance with other imaging techniques was done using 10 T1-weighted GE images, which all showed a satisfying reduction if the inhomogeneities after correction. Thus, it can be expected that the algorithm will perform in a similarly satisfying way for a vast variety of sequences, as long as the signal of the AT is high and the contrast between AT and remaining tissues is high enough (remaining tissue

classes have at maximum 70% of the AT class's intensity), which should be met in AT quantification procedures.

In conclusion, we developed an algorithm, which is able to reliably compensate for severe intensity inhomogeneities in abdominal, cross-sectional image slices. The algorithm itself does not require the adaption of any parameters when the bias field amplitude or its smoothness changes. Therefore, it can be used to compensate artificial spatial signal inhomogeneities, caused by different sources, such as RF interferences and spatial dependence of receiver coil sensitivity. Although the algorithm was developed in the context of VAT quantification, other applications that require highly homogeneous abdominal cross-sections, such as liver-fat-fraction mapping or the volumetry of organs, are possible applications.

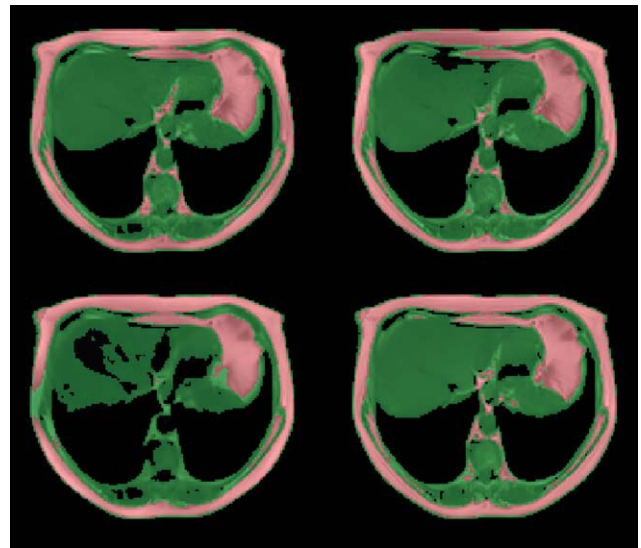


**Figure 10.** Example for the correction and classification (green: LT, red: AT) of a T1-weighted abdominal SE images: Gold standard, obtained by manual IHH compensation (a) uncorrected image (b) image corrected with LEMS, partly merging liver and lungs (BG) (c) image corrected with BC-FAT (d).

## REFERENCES

1. Obesity: preventing and managing the global epidemic. Report of a WHO consultation. World Health Organ Tech Rep Ser 2000; 894:i-xii, 1-253.
2. Hedley AA, Ogden CL, Johnson CL, Carroll MD, Curtin LR, Flegal KM. Prevalence of overweight and obesity among US children, adolescents, and adults, 1999-2002. *JAMA* 2004;291:2847-2850.
3. Chan DC, Watts GF, Barrett PH, Burke V. Waist circumference, waist-to-hip ratio and body mass index as predictors of adipose tissue compartments in men. *Q J Med* 2003;96:441-447.
4. Brodie DA, Stewart AD. Body composition measurement: a hierarchy of methods. *J Pediatr Endocrinol Metab* 1999;12:801-816.
5. Ohlson LO, Larsson B, Svardsudd K, et al. The influence of body fat distribution on the incidence of diabetes mellitus. 13.5 years of follow-up of the participants in the study of men born in 1913. *Diabetes* 1985;34:1055-1058.
6. Wajchenberg BL. Subcutaneous and visceral adipose tissue: their relation to the metabolic syndrome. *Endocr Rev* 2000;21:697-738.
7. Carr MC, Brunzell JD. Abdominal obesity and dyslipidemia in the metabolic syndrome: importance of type 2 diabetes and familial combined hyperlipidemia in coronary artery disease risk. *J Clin Endocrinol Metab* 2004;89:2601-2607.
8. Kissebah AH, Vydelingum N, Murray R, et al. Relation of body fat distribution to metabolic complications of obesity. *J Clin Endocrinol Metab* 1982;54:254-260.
9. Krotkiewski M, Bjorntorp P, Sjostrom L, Smith U. Impact of obesity on metabolism in men and women. Importance of regional adipose tissue distribution. *J Clin Invest* 1983;72:1150-1162.
10. Abate N, Burns D, Peshock RM, Garg A, Grundy SM. Estimation of adipose tissue mass by magnetic resonance imaging: validation against dissection in human cadavers. *J Lipid Res* 1994;35:1490-1496.
11. Shen W, Wang Z, Punyanita M, et al. Adipose tissue quantification by imaging methods: a proposed classification. *Obes Res* 2003;11:5-16.
12. Machann J, Thamer C, Schnoedt B, et al. Standardized assessment of whole body adipose tissue topography by MRI. *J Magn Reson Imaging* 2005;21:455-462.
13. Poll LW, Wittsack HJ, Koch JA, et al. Quantification of total abdominal fat volumes using magnetic resonance imaging. *Eur J Med Res* 2002;7:347-352.
14. Positano V, Gastaldelli A, Sironi AM, Santarelli MF, Lombardi M, Landini L. An accurate and robust method for unsupervised assessment of abdominal fat by MRI. *J Magn Reson Imaging* 2004;20:684-689.
15. Kullberg J, Ahlstrom H, Johansson L, Frimmel H. Automated and reproducible segmentation of visceral and subcutaneous adipose tissue from abdominal MRI. *Int J Obes (Lond)* 2007;31:1806-1817.
16. Würslin C, Springer F, Eibofner F, Schick F. Accurate adipose tissue segmentation from single gradient echo phase images by adaptive local thresholding. In: Proceedings of the 18th Annual Meeting of ISMRM, Stockholm, 2010. (abstract 5117).
17. Kullberg J, Johansson L, Ahlstrom H, et al. Automated assessment of whole-body adipose tissue depots from continuously moving bed MRI: a feasibility study. *J Magn Reson Imaging* 2009;30:185-193.
18. Reeder SB, Wen Z, Yu H, et al. Multicoil Dixon chemical species separation with an iterative least-squares estimation method. *Magn Reson Med* 2004;51:35-45.
19. Peng Q, McColl RW, Ding Y, Wang J, Chia JM, Weatherall PT. Automated method for accurate abdominal fat quantification on water-saturated magnetic resonance images. *J Magn Reson Imaging* 2007;26:738-746.
20. Würslin C, Machann J, Rempp H, Claussen C, Yang B, Schick F. Topography mapping of whole body adipose tissue using a fully automated and standardized procedure. *J Magn Reson Imaging* 2010;31:430-439.
21. Liou TH, Chan WP, Pan LC, Lin PW, Chou P, Chen CH. Fully automated large-scale assessment of visceral and subcutaneous abdominal adipose tissue by magnetic resonance imaging. *Int J Obes (Lond)* 2006;30:844-852.
22. Kullberg J, Angelhed JE, Lonn L, et al. Whole-body T1 mapping improves the definition of adipose tissue: consequences for automated image analysis. *J Magn Reson Imaging* 2006;24:394-401.
23. Positano V, Cusi K, Santarelli MF, et al. Automatic correction of intensity inhomogeneities improves unsupervised assessment of abdominal fat by MRI. *J Magn Reson Imaging* 2008;28:403-410.
24. Liew AW, Yan H. An adaptive spatial fuzzy clustering algorithm for 3-D MR image segmentation. *IEEE Trans Med Imaging* 2003;22:1063-1075.
25. Pham DL, Prince JL. Adaptive fuzzy segmentation of magnetic resonance images. *IEEE Trans Med Imaging* 1999;18:737-752.
26. Hayes CE, Mathis CM, Yuan C. Surface coil phased arrays for high-resolution imaging of the carotid arteries. *J Magn Reson Imaging* 1996;6:109-112.
27. Salvado O, Hillenbrand C, Zhang S, Wilson DL. Method to correct intensity inhomogeneity in MR images for atherosclerosis characterization. *IEEE Trans Med Imaging* 2006;25:539-552.
28. Schick F. Whole-body MRI at high field: technical limits and clinical potential. *Eur Radiol* 2005;15:946-959.
29. Machann J, Schlemmer HP, Schick F. Technical challenges and opportunities of whole-body magnetic resonance imaging at 3T. *Phys Med* 2008;24:63-70.
30. Kass M, Witkin A, Terzopoulos D. Snakes: active contour models. *Int J Comput Vis* 1988;1:321-331.
31. Cohen LD. On active contour models and balloons. *GVGIP: Image Underst* 1991;53:211-218.